Assimilation of SMOS brightness temperature into a large-scale distributed conceptual hydrological model.

Renaud Hostache[1], Dominik Rains[2,3], Kaniska Mallick[1], Marco Chini[1], Ramona Pelich[1],
Hans Lievens[2,4], Fabrizio Fenicia[5], Giovanni Corato[1], Niko E.C. Verhoest[2], and Patrick Matgen[1]

[1]Luxembourg Institute of Science and Technology (LIST), Department Environmental Research and Innovation, Belvaux, Luxembourg
[2]Ghent University, Department of environment, Ghent, Belgium
[3]University of Leicester, Earth Observation Science, Department of Physics & Astronomy, Leicester, UK
[4]KU Leuven, Department of Earth and Environmental Sciences, Heverlee, Belgium
[5]Swiss Federal Institute of Aquatic Science and Technology (EAWAG), Department Systems Analysis, Integrated Assessment and Modelling, Dübendorf, Switzerland

Correspondence: Renaud Hostache (renaud.hostache@list.lu)

Abstract.

The main objective of this study is to investigate how brightness temperature observations from satellite microwave sensors may help in reducing errors and uncertainties in soil moisture simulations with a large-scale conceptual hydro-meteorological model. In particular, we use as forcings the ERA-Interim public dataset and we couple the CMEM radiative transfer model with a hydro-meteorological model enabling therefore soil moisture and SMOS-like brightness temperature simulations. The hydro-meteorological model is configured using recent developments of the SUPERFLEX framework, which enables tailoring the model structure to the specific needs of the application as well as to data availability and computational requirements. In this case, the model spatial resolution is adapted to the spatial grid of the satellite data, and the soil stratification is tailored to the satellite datasets to be assimilated and the forcing data. The hydrological model is first calibrated using a sample of SMOS brightness temperature observations (period 2010-2011). Next, SMOS-derived brightness temperature observations are sequentially assimilated into the coupled SUPERFLEX-CMEM model (period 2010-2015). For this experiment, a Local Ensemble Transform Kalman Filter is used and the meteorological forcings (ERA interim-based rainfall, air and soil temperature) are perturbed to generate a background ensemble. Each time a SMOS observation is available, the SUPERFLEX state variables related to the water content in the various soil layers are updated and the model simulations are resumed until the next SMOS observation becomes available. Our empirical results show that the SUPERFLEX-CMEM modelling chain is capable of predicting soil moisture at a performance level similar to that obtained for the same study area and with a quasi-identical experimental set up using the CLM land surface model. This shows that a simple model, when carefully calibrated, can yield performance level similar to that of a much more complex model. The correlation between simulated and *in situ* observed soil moisture ranges from 0.62 to 0.72. The assimilation of SMOS brightness temperature observation into the SUPERFLEX-CMEM modelling chain improves the correlation between predicted and *in situ* observed soil moisture by 0.03 on average showing improvements similar to those obtained using the CLM land surface model.

1   Introduction

Motivated by the impact of climate change on the scarcity or excess of water in many areas around the world, and following the recommendations of the Sendaï framework for disaster risk reduction (UNISDR, 2015), several agencies and research
5 institutions have put substantial efforts in better monitoring and predicting the hydrologic cycle at a global scale. Such monitoring/prediction efforts are indeed necessary for assessing the risk of extreme hydrological events and for enabling flood and drought early warnings (Revilla-Romero et al., 2016), especially considering that impacts related to such hydrological extremes are expected to increase in the future due to the combined effect of socio-economic development and climate change (Lehner et al., 2016).

10 Numerical models such as hydrological and land surface models are central to predict and forecast floods and droughts (Matgen et al., 2012; Rains et al., 2017). They help in better anticipating disaster and the associated emergency response (Revilla-Romero et al., 2016). However, model simulations suffer from inherent uncertainties (Liu and Gupta, 2007), due to the simplified representation of physical processes as well as uncertain forcing (García-Pintado et al., 2015; Hostache et al., 2011) and the lack of data for setting up and controlling them (Pappenberger et al., 2007; Hostache et al., 2015; Wood et al.,
15 2016). To reduce uncertainty in model simulations, an advanced solution that has gained increased interest over the last decades is the integration of remote sensing data into models (Andreadis and Schumann, 2014; Hostache et al., 2018; De Lannoy and Reichle, 2016b). This approach pursues an optimal combination of hydro-meteorological modelling and remote sensing, for example by using satellite measurements as forcing or calibration data and/or for regularly updating the model states or parameters (Moradkhani, 2007). This allows periodically controlling and correcting the models via external observations. In
20 forecasting mode, such data assimilation approaches allow keeping the predictions on track, while in hind-casting mode they enable improved simulations of measured fluxes and states of the past.

Many advances have been made in these areas of research and undoubtedly, the near future will witness further progress as a result of the ever increasing number of spaceborne sensors enabling the large scale monitoring of key hydrological variables at unprecedented temporal and spatial resolution. In this context, spaceborne sensors are already providing a wealth of earth
25 observation data with many applications in hydrology (Brocca et al., 2012; De Lannoy and Reichle, 2016b). In particular, the last decades have seen the launch of several satellite missions allowing the monitoring of soil water storage and today, satellite soil moisture (SM) estimates are available at temporal and spatial resolutions compatible with operational hydrology requirements especially at the large scale (De Lannoy and Reichle, 2016b). Although the assimilation of *in situ* data is widely established in operational hydrology (Ercolani and Castelli, 2017), the assimilation of remotely sensed datasets, such as SM,
30 is a more recent development as this source of data has become available only over the last decades (e.g., Parada and Liang, 2004; De Lannoy et al., 2007; Jia et al., 2009; Matgen et al., 2012; Chen et al., 2014; Mohanty et al., 2017).

SM is a key variable in hydrological models. In many of them, including VIC, HBV, GR4J, etc., SM controls the partitioning of water and energy fluxes. Hence, improving its representation within a numerical model has the potential of improving

predictions of the key hydrological variables. In this context, SM data derived from various satellite missions such as ASCAT (e.g., Brocca et al., 2010, 2012; Dharssi et al., 2011; Draper et al., 2011) and AMSR-E (e.g., Reichle et al., 2007; Yang et al., 2007; Draper et al., 2009) have been assimilated into land surface or hydrological models (e.g., Draper et al., 2012; Renzullo et al., 2014).

5   Since November 2019, the passive Microwave Imaging Radiometer with Aperture Synthesis (MIRAS) onboard the Soil Moisture and Ocean Salinity (SMOS) satellite is observing top-of-the-atmosphere brightness temperature (Tb). The MIRAS sensor is sensitive to 1.4 GHz (L-band) emissions and takes multi-angular measurements at vertical and horizontal polarisations (Kerr et al., 2001). The algorithm used for the retrieval of SM values from SMOS Tb is based on land surface modelling (Kerr et al., 2012). In past studies, SM estimates retrieved from SMOS Tb were most of the time assimilated into land surface (e.g.,

10   De Lannoy and Reichle, 2016a; Lievens et al., 2016; Rains et al., 2017) and sometimes in conceptual hydrological models (e.g., Wanders et al., 2014; Lü et al., 2016). However, the land surface model used for the SM retrieval and the model used for the background simulation are often different. This potentially leads to differences in terms of process representation, model structure and model forcings (e.g., air and soil temperature) between the two models (De Lannoy and Reichle, 2016a). In the event the background simulation is carried out using a conceptual hydrological model, these differences may be even more

15   important, especially in terms of process representation. This potentially makes SM simulations and retrievals inconsistent and this can lead to a correlation between retrieved and simulated SM errors that cannot be easily handled by data assimilation filters (De Lannoy and Reichle, 2016b). As a consequence, recent studies (e.g., De Lannoy and Reichle, 2016a; Lievens et al., 2016; Rains et al., 2017) have aimed to directly assimilate SMOS Tb into such land surface models. To do so, these studies used as observation operator of the assimilation filter a radiative transfer model (e.g., the Community Microwave Emission

20   Modelling platform (CMEM), de Rosnay et al., 2009) that allows to derive SMOS-like Tb from SM simulations. In this context, De Lannoy and Reichle (2016a) showed that assimilating either SM retrievals or observed Tb yields almost the same correlation level between *in situ*-observed and simulated SM (average correlation equals 0.6 based on the records obtained from many measurement sites distributed across the United States of America).

Currently, for applications at the large scale, there is a tendency to rely on more complex physically-based hydrological

25   models in order to better capture the hydrological processes at hand (Devia et al., 2015). However, this may be sometimes detrimental to large-scale operational hydrology, due to the increased computational demand and the potential unavailability of the required datasets. In this context, conceptual models that allow for more efficient and rapid simulations offer an alternative to more physically-based land surface models (Devia et al., 2015; El Hassan et al., 2013). The main argument against the use of a conceptual model is often the need for site-specific parameter calibration that is often infeasible in data scarce areas. However,

30   with the recent increase of satellite missions providing global observations of key hydrological variables at high temporal and spatial resolution, it becomes possible to envisage the calibration of conceptual models even at the large scale. Hence, a science question that is worth investigating is whether a flexible conceptual model, relying on parameter calibration, can reach the performance level of a more complex physically-based model for hydrological simulations at large scales. Following the study by Rains et al. (2017), we evaluate here the potential of SMOS Tb assimilation for improving SM simulations of a distributed

35   conceptual hydrological model.

The SUPERFLEX modelling framework (Fenicia et al., 2016) enables tailoring the structure for the specific needs of the application. In particular, here we seek for a simplified representation of the main controlling processes, and computational efficiency in order to perform rapid simulations over large areas and for long periods. Compared to more physically based land surface models, the model built with SUPERFLEX offers fast running simulations without the need for high performance

5 computing facilities and allows for adapting the model spatial resolution and soil stratification to the characteristics of the satellite datasets that are to be assimilated.

The general objective of this study is to assess the performance of a soil moisture prediction chain based on the assimilation of SMOS Tb into a coupled SUPERFLEX-CMEM model and compare it to the one developed in Rains et al. (2017) based on the CLM land surface model. To enable a fair and meaningful evaluation and comparison, we use a quasi-identical experimental

10 set up to the one of Rains et al. (2017), except that we use here the SUPERFLEX instead of the CLM model to simulate soil moisture. As a test case, we use the Murray-Darling basin in Australia and we simulate distributed time series of soil moisture over the period 2010-2015.

The specific objectives of this study are as follows: (i) to compare the SUPERFLEX and CLM models in their ability to simulate SMOS-like Tb and soil moisture, and (ii) to evaluate the improvement in model predictions when assimilating SMOS

15 Tb observations.

In the next sections, we first present the database used for the experiment, the coupling between the hydrological (SUPERFLEX) and the radiative transfer (CMEM) models and the data assimilation experiment. Next, we calibrate the hydrological model using SMOS Tb observations, we evaluate the forward run of the SUPERFLEX-CMEM prediction chain and we compare the performances with the ones obtained in Rains et al. (2017). Then, we assess and discuss the results of the assimilation

20 experiment using the study by Rains et al. (2017) as a benchmark. As a further discussion element, we finally evaluate the impact of the assimilation of SMOS Tb on evapotranspiration simulations.

2   Material and Method

2.1   Study area and available data

2.1.1   Study Area

25 The study area is the Murray-Darling Basin (MDB) in South-Western Australia. The three main rivers of the MDB, namely rivers Darling, Murray and Murrumbigee are among the longest rivers in Australia. The MDB covers an area of more than 1 million km^2, representing approximately 14 % of the land surface of Australia. Due to its large dimensions, the basin exhibits various climate regimes, from sub-tropical in the north to semi-arid in the west and mostly temperate in the south. The average inter-annual rainfall ranges from up to 1,500 mm in the eastern side and less than 300 mm in the western side of the MDB

30 (MDBA, 2018). The average inter-annual temperature ranges from ca. 10 °C in south-eastern and ca. 20 °C in western side of the MDB (MDBA, 2018).
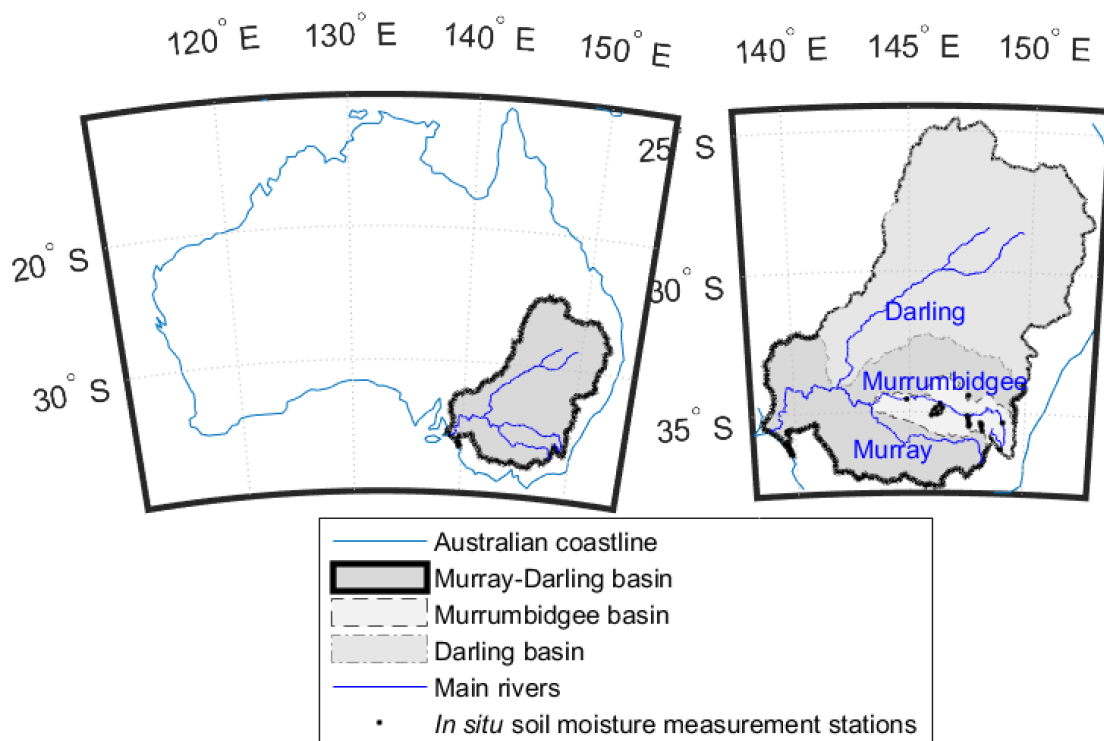
Figure 1. Study area: Murray-Darling Basin and *in situ* soil moisture measurement locations.

2.1.2 Meteorological forcings

Time series of rainfall and 2-m air and soil temperature predictions are globally available at a 3-hourly time step and 0.25° spatial resolution (downscaling from the original 0.75° spatial resolution) from the ERA-Interim reanalysis data set (Dee et al., 2011). From this data set, for each grid cell lying within the limits of the MDB, we extracted rainfall and soil and 2-m air

5 temperature for the period 2009 to 2016. Soil temperature was extracted for the two upper soil layers, having depths of 7 and 21 cm respectively. Next, the resulting time series were uniformly redistributed to an hourly time step. The potential evapotranspiration (PET) was estimated from the air temperature data using the Hamon formula (Hamon, 1963). Rainfall and PET time series are used as inputs of the SUPERFLEX hydrological model (see section 2.2.1). Soil and air temperature time series are used as inputs of the CMEM radiative transfer models (see section 2.2.2)

2.1.3 SMOS Tb observations

10

The SMOS database used in this study is identical to the one used in the study by Rains et al. (2017). It covers the period 2010 to 2015 and consists of SMOS Level 3 daily Tb at horizontal polarisation and 42.5° incidence angle. They are provided by the Centre Aval de Traitement des Données (CATDS) (version 310). SMOS acquisitions having probabilities of radio frequency

interference (RFI) greater than 0.2, Data Quality Index higher than 0.07 or activated science flags, namely strong topography, snow, flooding, urban areas, coastal zone and precipitation were filtered out from the initial database. The filtered observation data were resampled from the Equal-Area Scalable Earth Grid 2 (EASE2) 25 km grid to the $0.25°$ model grid used in the ERA-interim dataset by using inverse-distance interpolation.

2.1.4 *In situ* soil moisture observations

As an independent dataset for evaluating the model results, we make use of *in situ* soil moisture measurements from OzNet and CosmOz measurement networks (Smith et al., 2012). These datasets provide time series of soil moisture acquired using, respectively, time-domain reflectometry (TDR) probes and cosmic-ray neutron probes. Depending on the type of probe, soil moisture observations are available for various soil depths, namely 5, 8, 30, 60 and 90 cm. The measurement stations are mainly located within the Murrumbidgee catchment as the latter was selected as one of the sites for SMOS calibration/validation campaigns (Peischl et al., 2012). More details on the measurement techniques and the measurement network are provided in Rains et al. (2017), Renzullo et al. (2014), Holgate et al. (2016) and Su et al. (2013). It is worth mentioning that the *in situ* soil moisture dataset is provided with local or limited measurement footprints (a few hundreds of m^2 at maximum) whereas the hydrological model simulates average soil moisture over much larger areas (a few hundreds of km^2). As a consequence, the comparison between model results and *in situ* observation necessarily suffers from scale-representativeness issues.

2.1.5 *In situ* flux tower measurements

As an additional independent dataset for evaluating the model results, we also make use of *in situ* flux tower measurements from the TERN OzFlux measurement network (http://www.ozflux.org.au/). This dataset provides, among other variables, time series of latent heat fluxes that were converted into actual evapotranspiration rates using the latent heat of vaporization constant. The measurement stations are mainly located in the southern part of the MDB. Moreover, the *in situ* evaporation data, just like the previously described soil moisture data, are provided with local or limited measurement footprints.

2.2 The soil moisture and SMOS-like Tb prediction chain

2.2.1 The conceptual hydrological Model

The SUPERFLEX modelling framework (hereafter denoted SFX, Fenicia et al., 2011, 2016) is used to build the hydrological model. This modelling framework was developed with the aim to facilitate model development and allow model structure comparisons. The modelling platform is based on generic building components that can be configured and combined in various ways to generate different model architectures. Hydrologists can therefore hypothesize, build and test different model structures. For example, it allows for adapting the model structure to the forcing and observation datasets (e.g., in terms of spatial and vertical resolutions) and specific characteristics of the catchment. In the context of this study, we take advantage of this flexibility and define the model architecture in such a way that it allows to easily ingest globally available meteorological

forcing data and at the same time integrate Tb as observed by the SMOS satellite. The model is therefore distributed over grid cells of $0.25°$ matching the one used in the ERA-Interim dataset.

The architecture of the developed model is represented in Figure 2 for one model grid cell. It is mainly composed of two stratified upper root zone layers represented by two reservoirs, namely URu and URl. The grey box in Figure 2 also identifies the deeper reservoirs and the routing function that simulates surface runoff based on deeper soil layer water storage. In this study, since we focus on the two upper root zone layers that are of interest for simulating soil moisture, the deeper reservoirs and the routing function are not further referred to in the remainder.
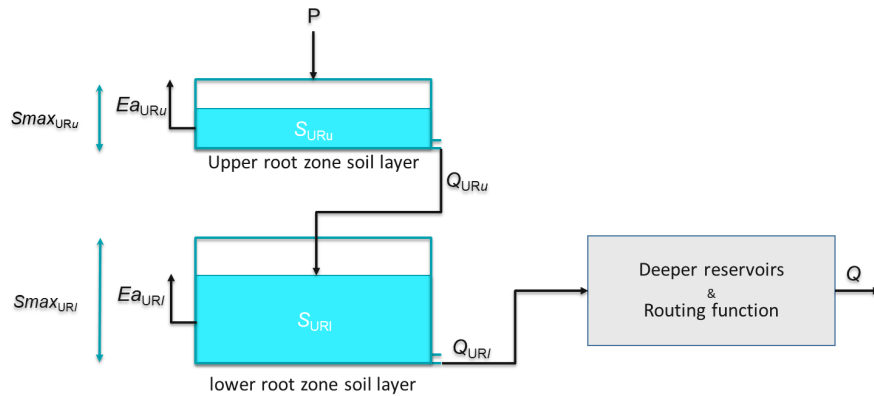

Figure 2. SUPERFLEX Model architecture.

The upper reservoir (URu) is fed by precipitation and loses water through evapotranspiration to the atmosphere and percolation to the second reservoir (**URl**). The latter is then fed by the incoming percolation from the first reservoir and loses water through evapotranspiration to the atmosphere and percolation to deeper soil. Outflow Q from the two root zone layers is estimated based on the simulated storage S and the incoming water amount using a power function with exponent α:

$$Q_{\mathrm{UR}x,i}(t) = P_i(t) \times \left(\frac{S_{\mathrm{UR}x,i}(t)}{Smax_{\mathrm{UR}x,i}} \right)^{\alpha_{\mathrm{UR}x,i}} \tag{1}$$

where t is time, i represents the model grid cell number, x stands for upper (u) or lower (l) reservoir, P is the input to the reservoir (precipitation for the upper reservoir, outflow from the upper reservoir for the lower reservoir), and $Smax$ is a parameter representing maximum storage capacity.

The actual evapotranspiration (Ea) from the two soil layers is estimated based on the simulated storage within the considered reservoir and the potential evapotranspiration (Ep) using a power function with exponent β:

$$Ea_{\mathrm{UR}x,i}(t) = Ep_i(t) \times \left(\frac{S_{\mathrm{UR}x,i}(t)}{Smax_{\mathrm{UR}u,i} + Smax_{\mathrm{UR}l,i}} \right)^{\beta_{\mathrm{UR}x,i}} \tag{2}$$

The variation of storage within the two reservoirs is estimated by solving the water balance equation:

$$\frac{\mathrm{d}S_{\mathrm{UR}x,i}(t)}{\mathrm{d}t} = P_i(t) - Q_{\mathrm{UR}x,i}(t) - Ea_{\mathrm{UR}x,i}(t) \tag{3}$$

For each reservoir, the soil moisture is derived from the storage according to:

$$\theta_{\mathrm{UR}x,i}(t) = C_{\mathrm{EF}x,i} \frac{S_{\mathrm{UR}x,i}(t)}{Smax_{\mathrm{UR}x,i}} \tag{4}$$

where θ is the predicted soil moisture and C_{EF} a so-called effective field capacity.

In the model architecture, the two root zone reservoirs are meant to conceptually represent two stratified soil layers allowing

5 to simulate soil moisture over different soil depths. To maintain constant depths of these two layers over the model domain (namely 7 and 21 cm in accordance to the depth of the two upper soil layers depicted in the ERA-interim dataset) the respective reservoir maximum capacities are computed depending on the C_{EF} considering that the maximum storage capacity of a soil layer can be derived from the C_{EF} and the soil layer depth d according to:

$$Smax_{\mathrm{UR}x,i} = C_{\mathrm{EF}x,i} \times d_{\mathrm{EF}x} \tag{5}$$

10 It is worth noting here that the model structure presented beforehand is replicated on each model grid cell i. As a consequence, for each grid cell, the model has six calibration parameters, namely $C_{\mathrm{EF}u,i}$, $\alpha_{\mathrm{UR}u,i}$, $\beta_{\mathrm{UR}u,i}$, $C_{\mathrm{EF}l,i}$, $\alpha_{\mathrm{UR}l,i}$, $\beta_{\mathrm{UR}l,i}$. Moreover, the maximum storage capacities $Smax_{\mathrm{UR}x,i}$ are computed based on fixed soil layer depths $d_{\mathrm{EF}x}$ and calibrated effective field capacities $C_{\mathrm{EF}u,i}$.

2.2.2 The radiative transfer model

15 To simulate SMOS-like Tb using soil moisture predictions of the SFX hydrological model, we use the Community Microwave Emission Model version 5.1 (CMEM, de Rosnay et al., 2009).

The set up of CMEM in our study is identical to the one defined in the study of Rains et al. (2017) in order to enable a meaningful comparison between both experiments. In particular, the time invariant input data (i.e., soil sand and clay fractions, permanent water surface fractions, ground elevation and vegetation cover types) as well as the equations used to run CMEM

20 are exactly the same. The ECOCLIMAP vegetation classes (Champeaux et al., 2005) are used to provide CMEM with the plant functional types. The development cycle of vegetation classes is defined in CMEM based on the leaf area index (LAI) (Rains et al., 2017). LAI is interpolated at daily scale from a monthly dataset for low vegetation and a constant LAI value is fixed for high vegetation. The dielectric constant computation is carried out using the Mironov model (Mironov et al., 2004) and the required effective temperature is computed via the Wigneron model (Wigneron et al., 2001). The Fresnel, Choudhury

25 (Choudhury et al., 1979) and Wigneron (Wigneron et al., 2007) models are used for assessing smooth surface emissivity, soil roughness and vegetation opacity respectively. Atmospheric contributions are estimated via the Pellarin method (Pellarin et al., 2003).

The coupling between SFX and CMEM is quasi identical to the one set up in Rains et al. (2017) using CLM: the soil layer depths in CMEM are identical to the ones used in the SFX model to maintain inter-model consistency ; the soil moisture

30 simulated by SFX is used as input of CMEM and the 2 m air temperature is derived from the ERA-Interim dataset (Dee et al., 2011). However, as SFX does not integrate energy balance processes (while CLM does), it was necessary to slightly adapt the set up of Rains et al. (2017) and the soil temperature is in our experiment derived from the ERA-Interim dataset (Dee et al., 2011) whereas it is simulated by CLM in Rains et al. (2017).

2.2.3 Model Calibration

On each grid cell, the SFX model has 6 calibration parameters (see section 2.2.1). To carry out the calibration, Monte-Carlo simulations using latin hypercube sampling within plausible parameter ranges are carried out. To do so, parameter sets are first randomly generated within such plausible parameter ranges. Next, a SFX-CMEM simulation is carried out for each individual

5   parameter set and the simulated Tb is compared, at the grid cell scale, to the values derived from SMOS observations. Eventually, for each individual model grid cell, the parameter set yielding the lowest unbiased root mean square deviation ($ubRMSD$, Entekhabi et al., 2010, see Eq. 6) while comparing simulated and SMOS-derived Tb is selected as optimal. The $ubRMSD$ is chosen here has it allows to remove the bias between simulated and observed soil moisture (and Tb) which is common in brightness temperature assimilation studies.

10   $$ubRMSD = \sqrt{\left\langle \left((y^s(t) - \langle y^s \rangle_t) - (y^o(t) - \langle y^o \rangle_t) \right)^2 \right\rangle_t} \qquad (6)$$

where y^s is the simulated Tb and y^o the observed one and $\langle . \rangle_t$ indicates the average over time. The parameters of the CMEM model were not adjusted and their default values were used to keep the current experiment quasi identical to one of Rains et al. (2017).

2.3 Data Assimilation

15   ### 2.3.1 Data assimilation filter

In this section, we present the method used for assimilating SMOS Tb into the SFX-CMEM coupled models. The method proposed in this study uses as assimilation filter a Local Ensemble Transform Kalman Filter (LETKF) introduced by Hunt et al. (2007) and implemented by Miyoshi and Yamane (2007). As usual in ensemble Kalman filtering, the uncertainty in model predictions is represented via a set of k stochastic model realizations (k=32 in this experiment) having different perturbed

20   forcings and/or parameters and the model and observation errors are assumed to be normally distributed. The localisation is set up so that the assimilation is carried out at the model grid scale. The observation operator is linearly approximated during the analysis step in the LETKF (see Eq.18 in Hunt et al., 2007). As argued in Hunt et al. (2007), LETKF is deterministic as no additional random error is added to the observation. This is an advantage here as it allows us to keep track of the individual ensemble members during the assimilation. Let us denote our non-linear model $\mathcal{M}$, namely SFX, that propagates state variables

25   in time (including soil moisture θ) between two assimilation time steps (Eq. 7).

$$x_{n,j}^b = \mathcal{M}\left(x_{n-1,j}^a \right) \qquad (7)$$

where $x_{n,j}^b$ is the background at time t_n when the assimilation is supposed to be carried out for ensemble member number j, and $x_{n-1,j}^a$ is the analysis computed at time t_{n-1}, i.e. the previous assimilation time step.

The step prior to the assimilation is to run the hydrological model between t_{n-1} and t_n to yield the background ensemble. In our study, the application of the LETKF proposed by Hunt et al. (2007) consists of the seven main steps listed hereafter (please note that the temporal index n is not repeated later on for the sake of conciseness).

1. Apply the observation operator, namely CMEM, to the model background ensemble to form the observational background ensemble $y^{\mathrm{b}} = [y_1^{\mathrm{b}}, ..., y_k^{\mathrm{b}}]$.

2. Compute the ensemble observational background perturbations based on the ensemble mean $\overline{y^b}$:

$$\mathbf{Y}^{\mathrm{b}} = [y_1^{\mathrm{b}} - \overline{y^{\mathrm{b}}}, ..., y_k^{\mathrm{b}} - \overline{y^{\mathrm{b}}}]$$

3. Compute the ensemble background perturbations based on ensemble mean $\overline{x^b}$:

$$\mathbf{X}^{\mathrm{b}} = [x_1^{\mathrm{b}} - \overline{x^{\mathrm{b}}}, ..., x_k^{\mathrm{b}} - \overline{x^{\mathrm{b}}}]$$

4. Compute the matrix $\tilde{\mathbf{P}}^a = \left[(k-1)\mathbf{I} + \left(\mathbf{Y}^{\mathrm{b}}\right)^T \mathbf{R}^{-1}\mathbf{Y}^{\mathrm{b}} \right]^{-1}$ where $\mathbf{I}$ is the identity matrix and $\mathbf{R}$ the observation error covariance matrix.

5. Compute the matrix $\mathbf{W}^{\mathrm{a}} = \left[(k-1)\tilde{\mathbf{P}}^{\mathrm{a}} \right]^{1/2}$

6. Compute the k-dimensionnal vector $\overline{w}^{\mathrm{a}} = \tilde{\mathbf{P}}^{\mathrm{a}} \left(\mathbf{Y}^{\mathrm{b}}\right)^T \mathbf{R}^{-1} \left(y^o - \overline{y}^{\mathrm{b}}\right)$ and derive w_j^{a} by adding $\overline{w}^{\mathrm{a}}$ to each column of $\mathbf{W}^{\mathrm{a}}$

7. Compute the individual member analysis $x_j^{\mathrm{a}} = \overline{x}^{\mathrm{b}} + \mathbf{X}^{\mathrm{b}}\mathbf{w}_j^{\mathrm{a}}$

This process is repeated for each cell of the model domain where a SMOS observation is available at time step t_n. Once the analysis has been carried out, state variables, namely the storage in the two soil layers of SFX (section 2.3.1), are updated and the simulation is resumed until the next assimilation time step.

As mentioned in many studies dealing with the assimilation of satellite SM or Tb (e.g. Al Bitar et al., 2012; Matgen et al., 2012; Rains et al., 2017; Al-Yaari et al., 2017), bias removal prior to the assimilation is often a necessary step. In our study, we reduce the bias between simulations and observations by deriving model and observation anomalies, following an identical approach to the one described in Rains et al. (2017). Anomalies are defined as the difference between the original Tb time series and their inter-annual climatologies (time-average SMOS observation acquired in a 20 days-sliding window centred on the considered day of year). The climatology is computed by first smoothing the Tb time series using a 20-days moving average and next computing the inter-annual average of the smoothed signal. The model background used in the assimilation filter is the simulated Tb anomaly computed as the difference between the simulated Tb and its climatology, computed as the climatology of the ensemble mean of the open loop run. The data assimilation is therefore carried out based on the simulated and observed Tb anomalies.

2.3.2 Ensemble generation

To generate an ensemble of SMOS-like Tb, the meteorological forcings of the SFX-CMEM models derived from the ERA-interim dataset, namely the rainfall and the air and soil temperature time series are randomly perturbed. As in Rains et al. (2017), the perturbation applied to rainfall time series is multiplicative and randomly generated from a log-normal statistical distribution of mean 0 and standard deviation 0.5. The air temperature time series are perturbed using an additive Gaussian random noise of mean 0 K and standard deviation 2.5 K. Each time step and each model grid cell has an independently drawn random perturbation. Moreover, to maintain a set up similar to the one used in Rains et al. (2017) where air temperature perturbations are propagated to the soil temperature via the CLM model, perturbed soil temperature predictions are here drawn from the perturbed air temperature. This is done in two steps. First, linear regressions are carried out on each grid cell between the ERA-interim predictions of air temperature and soil temperature (separately for the two soil layers). Next, perturbed soil temperatures are derived from the perturbed air temperatures based on the coefficients obtained from the linear regressions. This allows to maintain a certain level of consistence between perturbed air and soil temperatures for each ensemble member. The main difference between our experiment and the one of Rains et al. (2017) is that we do not perturb soil texture as this parameter of CLM does not apply to SFX.

2.4 Analyses used to evaluate the proposed soil moisture prediction chain

The proposed modelling framework is evaluated and compared to the one proposed in Rains et al. (2017) using a series of empirical tests:

1. We assess the performance of the calibrated conceptual SFX model by comparing, via the Pearson's correlation, the RMSD and the mean bias, the simulated and observed SMOS Tb.

2. We compare SFX-based model performance to the one of the forward CLM model previously introduced in Rains et al. (2017). To do so, we make use of the RMSD and the Pearson's correlation together with Taylor diagrams computed based on the comparison between CLM (resp. SFX) model simulations and observations of Tb (SMOS observation) and SM (*in situ* measurements).

3. We assess the effect of the assimilation of SMOS Tb by comparing the open loop and the assimilation simulations of SM with *in situ* SM measurements, via the RMSD, the Pearson's correlation, the ubRMSD, the assimilation efficiency and Taylor diagrams and we analyse the spatial distribution of correlation improvement by mapping the changes in correlation between predictions and in situ measurements of soil moisture at each stations.

4. We further evaluate the influence of the assimilation of SMOS observations on the prediction of evapotranspiration by comparing the open loop and the assimilation simulation of evapotranspiration with *in situ* measurements.

3 Results and discussion

In this section, the performance of the conceptual SFX model is assessed and compared to the one of the physically-based CLM land surface model by comparing simulated and observed time series of Tb and soil moisture.

3.1 Evaluation of the calibrated SUPERFLEX hydrological model

5 Figure 3 shows the Pearson's correlation coefficient, the RMSD and the Mean Bias maps obtained by comparing SFX-simulated and SMOS-observed Tb time series periods and Table 1 the associated spatial statistics during the calibration (2010-2011) and the validation (2012-2015). From this figure and this table, the following results can be noted:

1. The calibrated model yield rather satisfying predictions of Tb. In addition, the obtained performances are comparable to those obtained in (Rains et al., 2017). In particular, in our study we have an average correlation of 0.7, an average

10 ubRMSD of 14.8 K and an average bias of 30.21 K during the validation period. In the study of Rains et al. (2017) using CLM, the RMSD has an average value of 30 K and the average correlation a value 0.7.

2. The three performance metrics have rather similar values and spatial variability when computed during the calibration and the validation periods although slight differences are visible in Table 1.

3. A general gradient of performance can be seen from the eastern to the western part of the basin.

15 4. The lowest performances are mainly exhibited on pixels located in the Darling river floodplain (Figure 1).

Results 1 and 2 leads us to conclude that model results are satisfactory in view of previous applications. Result 3 can be explained based on the fact that the hydrological regimes vary from east to west in the MDB. Whereas the eastern part is more dominated by important rainfalls, the western part receives limited amounts of rainfall and evapotranspiration plays then a more important role in the hydrological cycle. Considering that in our set up, the representation of the evapotranspiration is

20 rather simplistic as it is based on the Hamon formula, this could explain the poorer performance of the model in the western part of the basin. Result 4 can be explained considering that the input data used for running CMEM concerning the fraction of the grid cell covered by surface water. This input is considered invariant over time in our set up, while in reality an important number of lakes and ponds of the Darling river floodplain are periodically drying and filling up during the year, potentially modifying the water fraction on the corresponding model grid cells.

25 ### 3.2 Comparison of the performances of the SUPERFLEX and CLM models

To compare the SFX-based model performance to the one of the forward CLM model previously introduced in Rains et al. (2017), we first make use of Taylor diagrams (Figure 4). These represent useful tools to evaluate and inter-compare model performances as they display on a unique plot three key performance statistics, namely the normalized standard deviation of model results, the normalized root mean square deviation (RMSD) and the correlation between model predictions and

30 observations. The normalisation of standard deviation and RMSD is carried out with respect to observed time series statistics.
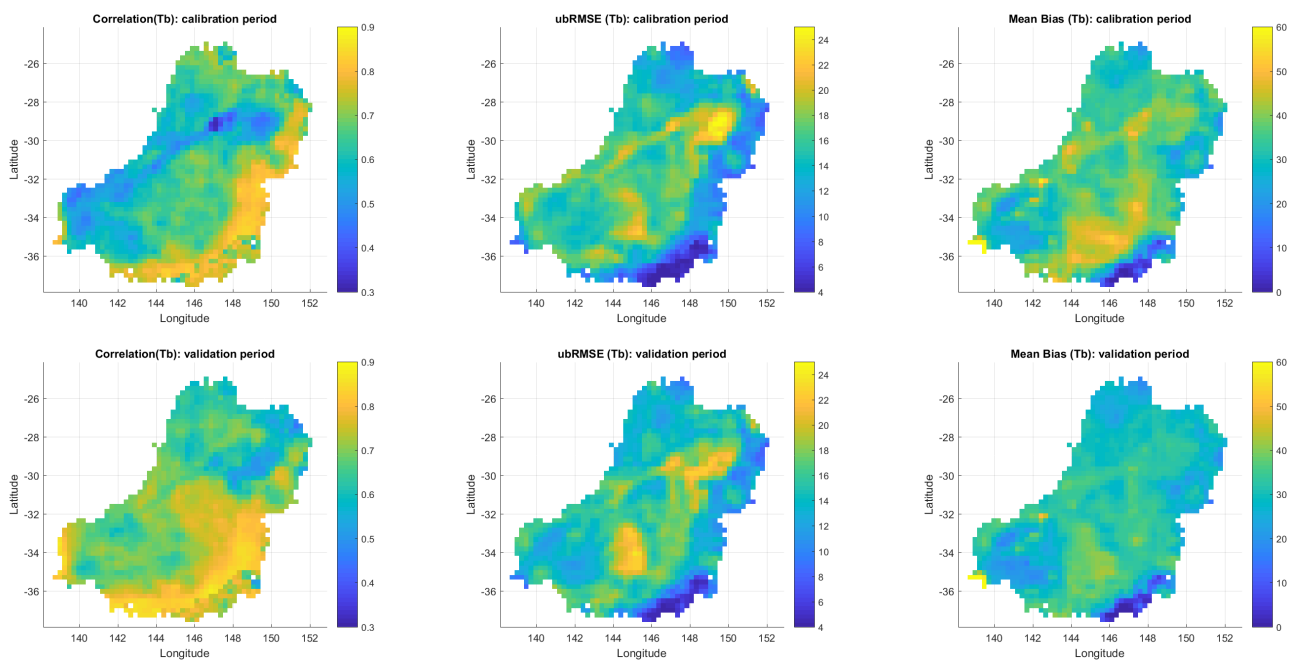
Figure 3. Peason's correlation coefficients (left hand side panels), Root mean square deviation (RMSD, center panels) and Mean Bias (right hand side panels) between SFX-CMEM predictions and SMOS observations of Tb during the calibration (top panels) and the validation (bottom panels) periods.

Table 1. Spatial statistics of simulated Tb performance metrics.

Spatial statistics	Correlation		ubRMSD		Mean Bias	
	Cal	Val	Cal	Val	Cal	Val
Mean	0.65	0.7	14.75	14.8	34.7	30.21
Median	0.65	0.69	15.31	14.86	35.37	31.02
Mode	0.32	0.44	3.91	4.25	0.1	-1.11
Skewness	-0.14	-0.08	-0.61	-0.4	-0.01	0.75
Kurtosis	2.78	2.78	3.67	3.98	12.06	23.54

The perfect model would therefore be a point located in the circle labelled as "0" in Figure 4 with values of normalized standard deviation, normalized RMSD and correlation respectively equal to 1, 0 and 1.

Figure 4 assumes that the SMOS Tb observations are reliable and accurate. The panel on the left hand side of Figure 4 shows the spatially averaged model statistics of both models during the calibration and the validation periods. As can be seen,
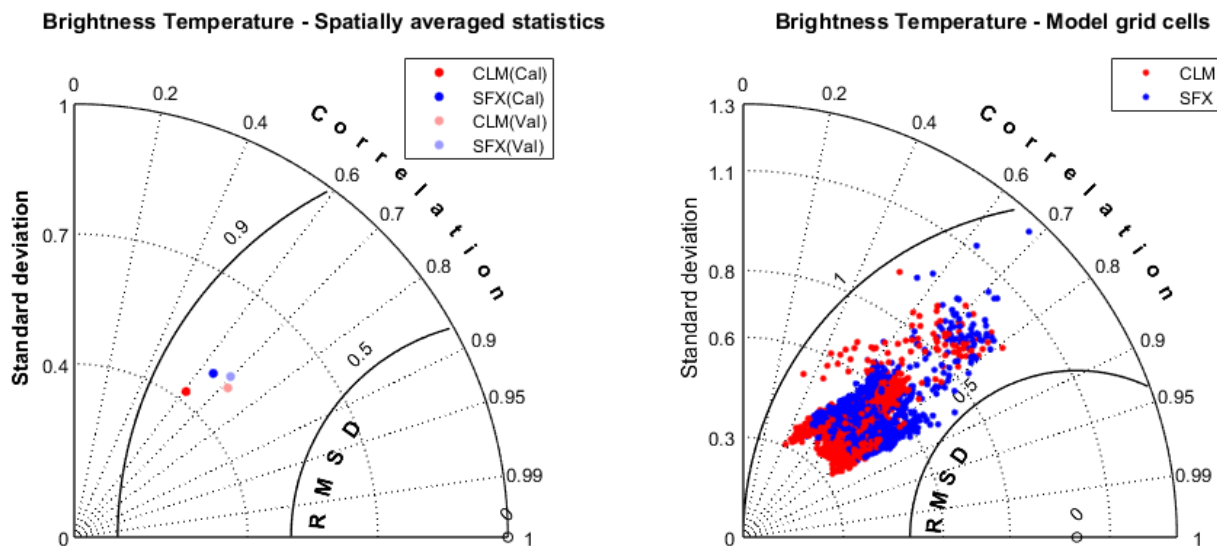
Figure 4. Taylor Diagrams (TD) based on the comparison between SMOS-observed and SFX- and CLM-simulated Tb respectively: TD drawn by spatially averaging model grid cell statistics, separating the calibration (cal) and validation (val) periods (left panel) and TD drawn using model grid cell statistics individually for calibration and validation periods together (right panel). Red dots indicate CLM statistics and blue dots SFX statistics.

the performances of both models are similar with average correlation ranging between 0.62 and 0.72 during the calibration and validation periods. Whereas SFX slightly outperforms CLM during the calibration period, CLM exhibits slightly better correlation during the validation period. Overall, both models yield very similar levels of satisfying performances. The performances obtained here are as well rather similar to the ones showed in De Lannoy and Reichle (2016a) with correlation between *in situ*-observed and simulated SM of 0.6 on average over many stations over the United States of America. One can notice that both models have a tendency to underestimate observed variance of Tb as normalized standard deviation values are lower than 1. The panel on the right hand side of Figure 4 shows the model performance for each individual model grid cell. The model statistics are here computed over the complete simulation period (calibration and validation periods). At the model grid cell scale, both model statistics cover a rather wide range of performance levels. This highlights the fact that both models, albeit yielding good overall levels of performance are less accurate for a few cells. Overall the performance metrics shown in Figure 4 confirm that the two models reach similar levels of performance.

Figure 5 shows the maps of difference in correlation and RMSD between both models, as well as the map of average hourly rainfall and PET. The top left hand side panel highlights a gradient in the difference in correlation from west to east: the SFX-predicted Tb is better correlated with SMOS observations in the Eastern part of the basin where precipitation is mainly controlling soil moisture dynamics (Figure 5, bottom left panel) and the CLM-predicted Tb is better correlated with SMOS observation in the Western part, where evapotranspiration is impacting soil moisture variations more significantly (Figure 5,

bottom right panel). This is arguably explained by a better representation of the evapotranspiration process in CLM and a better
capability of SFX to simulate fast transfer of rainfall to deeper soil layers at saturation. The top right hand side panel shows a
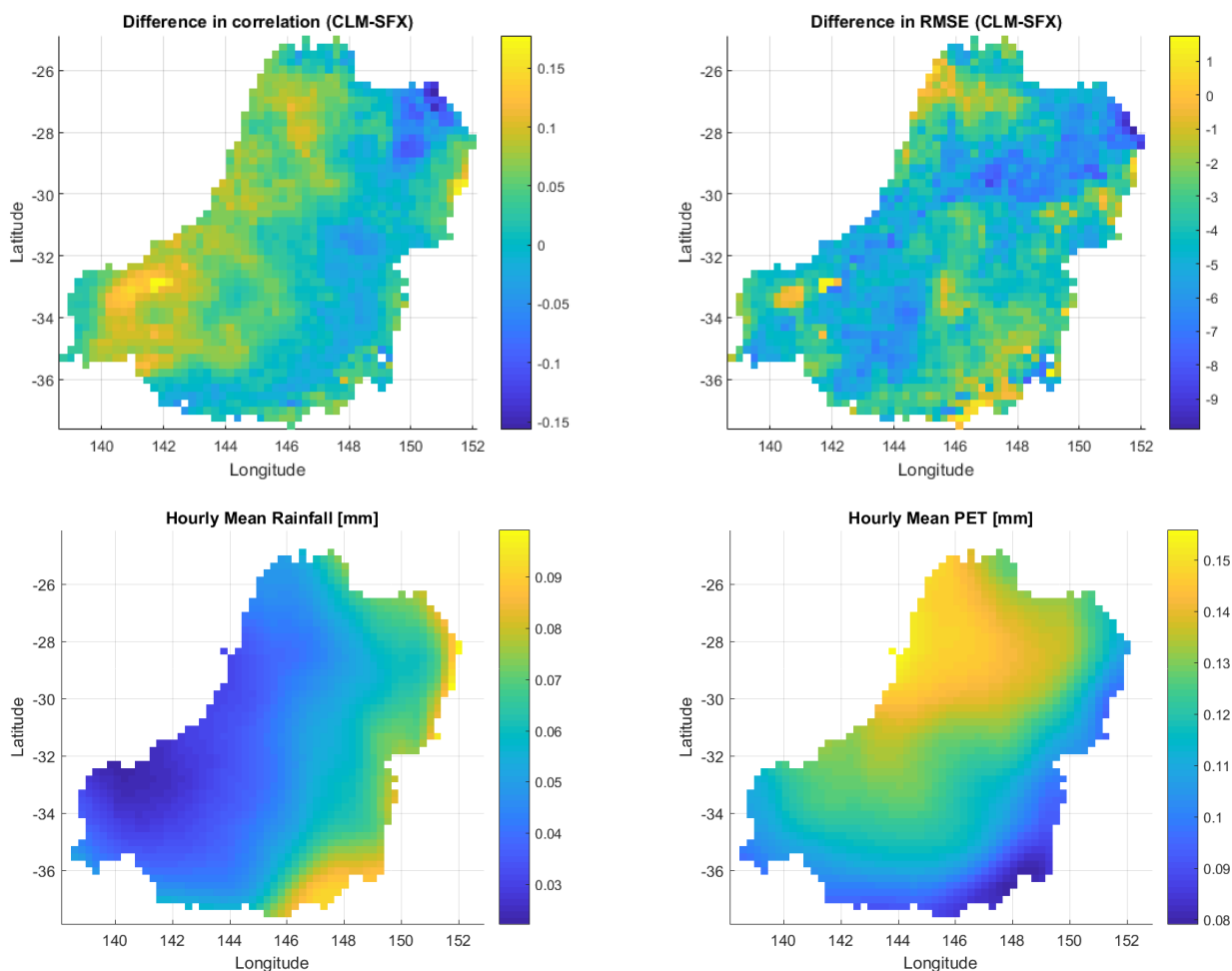generally higher deviation in SFX-based predictions of Tb.

Figure 5. Maps of differences in correlation (top left panel) and RMSD (top right panel) between CLM- and SFX-simulated Tb using as a
reference SMOS observation, and maps of hourly average of input Rainfall (bottom left panel) and PET (bottom right panel).

As SMOS observations likely suffer from significant uncertainties, we propose to further evaluate model results using *in situ*
observed soil moisture time series from a limited number of available measurement sites (Figure 1). In this context, Figure 6
shows the Taylor diagrams drawn from the comparison between time series of soil moisture observed and simulated by both
models for the thin upper soil layer (panel on the left hand side) and a deeper soil layer (panel on the right hand side). For the
thin upper soil layer (0-8 cm depth) the observations are directly compared with the soil moisture simulations of the upper SFX
reservoir. For the deeper soil layer (0-30 cm depth), the observations are compared with the average soil moisture predictions

computed as the weighted mean, with weighting proportional to the maximum storage capacity, of the upper and lower SFX reservoirs (see Figure 2).
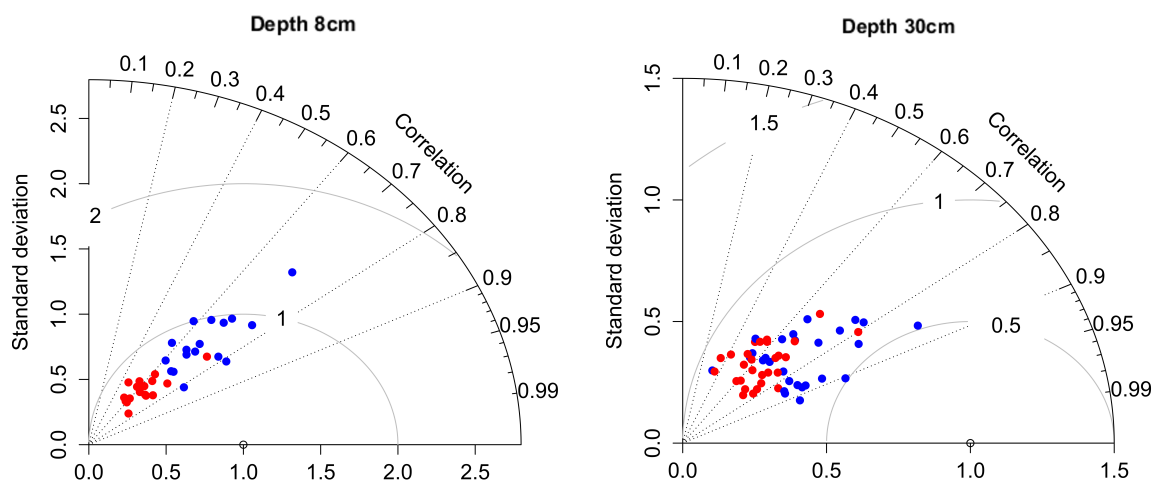

Figure 6. Taylor Diagrams (TD) drawn from the comparison between *in situ*-observed and SFX-simulated soil moisture for two different soil depth and the two different models. Blue dots indicate SFX statistics and red dots CLM statistics.

Both models exhibit similar correlations. For the upper soil layer, SFX is better in capturing the observation variance. Regarding the RMSD, CLM slightly outperforms SFX with sometimes lower values for the upper soil layer. For the deeper 5 soil layer, both models yield again similar performance levels with satisfying correlations, SFX slightly overperforming CLM.

As a conclusion on the comparison between the forward run of both models, it can be highlighted that the two models finally reach similar performance levels when using as a reference either observed SMOS Tb or *in situ* measured soil moisture. It is also important to keep in mind that similar performance levels have been attained provided that the SFX model was carefully calibrated.

10 ### 3.3 Effect of the assimilation of SMOS Tb on the SFX hydrological model

The data assimilation framework proposed in section 2.3 is applied over the period 2010-2015. Each time a SMOS observation is available over a model grid cell, the assimilation filter is applied on the background and the soil water storage variables of SFX are updated. We assimilated SMOS anomalies and the error covariance of the SMOS observation anomalies R is assumed constant and equal to 25 K^2. Table 2 reports the average performance metrics of the open loop (i.e., without assimilation) and 15 the analysis simulation performance metrics for two soil layer depths. As some model grid cells include several soil moisture measurement stations and with the objective to compensate for the limited footprint, the average performance metrics in Table 2 are computed both over the individual soil moisture measurement stations and over the cells where *in situ* observations are available. In the second case, all soil moisture observations available in a given model grid cell are first averaged. The performance metrics are next computed using as a reference the "averaged" observations. Eventually, the average metrics are

obtained by spatially averaging the model grid-cell based metrics. As can be seen in Table 2, the assimilation allows for a moderate increase in correlation for the two soil layers depicted in the model when comparing observed and simulated soil moisture time series. Specifically, the correlation increases on average by more than 0.03 for both soil layer depths. These improvements are similar to those obtained in the study by Rains et al. (2017, experiments DA2 and DA0), namely ca. 0.06

5 for upper layers and 0.03 for deeper layers. One possible explanation for the slightly lower improvements in correlation for the top-layer can be found in the SFX open-loop performance being already higher (correlation equals 0.77) than that of CLM (correlation equals 0.61). This arguably reduces the room for improvement as a result of the assimilation as the SFX-based open-loop outperforms the one based on CLM.

However, while correlations increase due to the positive effect of the assimilation, one can notice in Table 2 that errors

10 (RMSD and ubRMSD) tend to remain rather stable. This indicates that the assimilation improves the correlation between model predictions and observations, but fails in reducing average errors in our experiment. This result is consistent with the findings of Rains et al. (2017).

Table 2. Time-space average values of background and analysis performance (comparison with *in situ*-observed soil moisture).

Space averaging	Layer depth		Correlation	RMSD	ubRMSD
Over measurement stations	8cm	open loop	0.776	0.1	0.98
		analysis	0.801	0.1	0.98
	30cm	open loop	0.695	0.11	0.071
		analysis	0.727	0.11	0.072
Over model grid cells	8cm	open loop	0.771	0.1	0.099
		analysis	0.803	0.1	0.1
	30cm	background	0.695	0.11	0.062
		analysis	0.726	0.11	0.064

To evaluate the effect of the assimilation on individual measurement points, Figure 7 shows the Taylor diagrams obtained from the comparison between model predictions and *in situ* observations of soil moisture for two soil layer depths. In this

15 figure, the circles indicate the open loop run performances and the triangles the assimilation run performances. Each colour is assigned to an individual observation point. In Figure 7 almost every individual observation point exhibits an improvement in correlation due to the assimilation and this for both soil layers. More precisely, all correlations increase for the first layer and all correlation except one increase for the second soil layer. The improvement is however rather different from one point measurement to another. Figure 7 indicates that, in general, the lower the open loop run correlation, the higher the improvement.

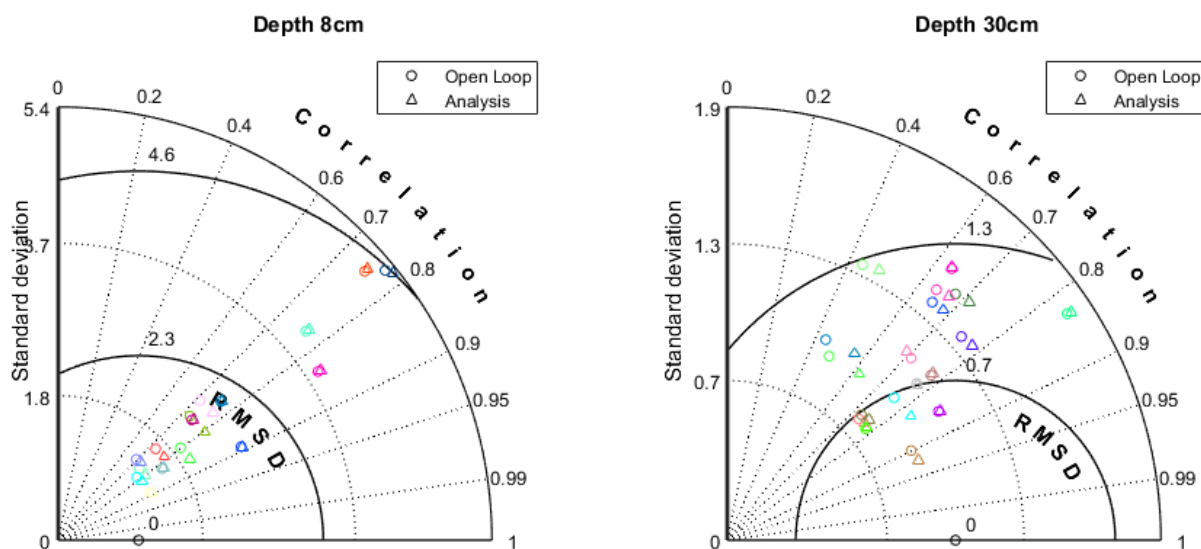20 This general feature is especially visible for the deeper soil layer.

Figure 7. Taylor Diagrams (TD) drawn from the comparison between *in situ*-observed and SFX-simulated (background and analysis) soil moisture for the two different soil depth.

To analyse the spatial distribution of correlation improvement as a result of the SMOS data assimilation, Figure 8 (top panels) maps the changes in correlation between predictions and *in situ* measurements of soil moisture at all stations. Especially for the first layer, one can notice a gradient from East to West within the Murrumbidgee basin (where observation sites are located). The bottom panels in Figure 8 show the climate variability over the Murrumbidgee catchment using as a proxy the average annual rainfall and PET (data provided by the Australian Bureau of Meteorology), together with the number of SMOS records assimilated over *in situ* soil moisture measurement sites. The two bottom panels in Figure 8 indicate that it is likely that the gradient in correlation increase has its origin in climate variability but that it also depends on the the number of SMOS observations that are locally assimilated (panel on the bottom left hand side). In the Western semi-arid Murrumbidgee, soil moisture updates tend to have a longer-lasting effect on the performance because evapotranspiration is the main soil moisture controlling process and because the extraction of water from the soil due to evapotranspiration takes much longer than soil recharge due to rainfall.

Overall, our experiment shows that the assimilation of SMOS data into the SFX model allows for a substantial improvement of the correlation between model predictions and *in situ* observations of soil moisture with improvements similar to those obtained in a very similar study by Rains et al. (2017) using the CLM land surface model.
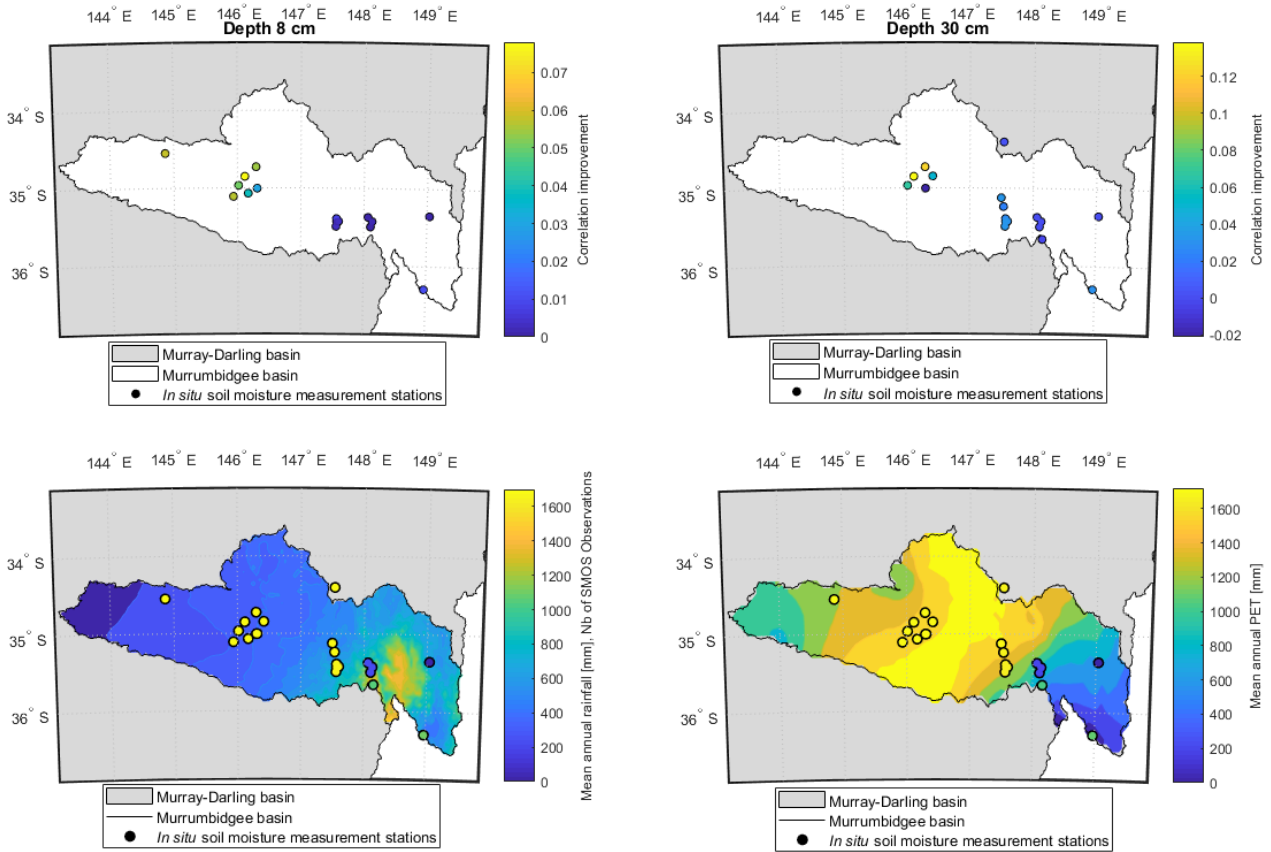
Figure 8. Correlation improvement in soil moisture prediction in relation to climate variability and number of assimilation events: Maps of the improvement in soil moisture correlation for the two root zone soil layers (upper panels) and maps of the number of assimilated SMOS Tb observation at each soil moisture measurement station, in relation with inter-annual average rainfall (bottom left panel) and inter-annual average PET (bottom right panel).

To further investigate the effect of the assimilation on soil moisture prediction errors, we compute a so-called assimilation efficiency:

$$
E(t_n) = \begin{cases} \left(1 - \dfrac{SD_{An}(t_n)}{SD_{OL}(t_n)}\right) * 100, & \text{if } SD_{An} \leq SD_{OL} \\[2ex] \left(\dfrac{SD_{OL}(t_n)}{SD_{An}(t_n)} - 1\right) * 100, & \text{if } SD_{An} > SD_{OL} \end{cases}
\tag{8}
$$

$$
\text{With} \begin{cases} SD_{OL}(t_n) = \sum\limits_{t=t_n}^{t_{n+1}-1} \left(\theta_{OL}(t) - \theta_{Obs}(t)\right)^2 \\[2ex] SD_{An}(t_n) = \sum\limits_{t=t_n}^{t_{n+1}-1} \left(\theta_{An}(t) - \theta_{Obs}(t)\right)^2 \end{cases}
$$

where $E(t_n)$ is the efficiency of the analysis at time step t_n, SD_{An} the squared deviation of the analysis run, SD_{OL} the squared deviation of the open loop run, θ_{Obs} the observed soil moisture, θ_{An} the analysis soil moisture prediction and θ_{OL} the open loop soil moisture prediction. The efficiency evaluates the squared deviation change as a result of the assimilation. Positive values indicate an error reduction, while negative ones indicate that the squared deviation increased after the analysis step.

5 In Figure 9, we plot the averaged efficiency as a function of the open-loop soil moisture prediction percentiles for two soil depths. To do so, we first compute, for each individual efficiency, the percentile of the synchronously obtained open loop soil moisture prediction and then compute the average efficiency for each percentile of the open loop soil moisture predictions. Figure 9 shows that the errors in soil moisture prediction are mainly reduced by the assimilation for the higher quantiles of soil moisture while they tend to increase for the lower quantiles. For the upper layer, the assimilation is more efficient for

10 predicted soil moisture values higher than the median. For the deeper layer, errors are reduced for quantiles higher than 80 %. This indicates that the assimilation is more efficient for high soil moisture states. A possible explanation for this is that the assimilation reduces errors when upper soil layers are closer to saturation, mainly during rainfall events when errors in ERA Interim rainfall simulations are arguably affected by larger errors.
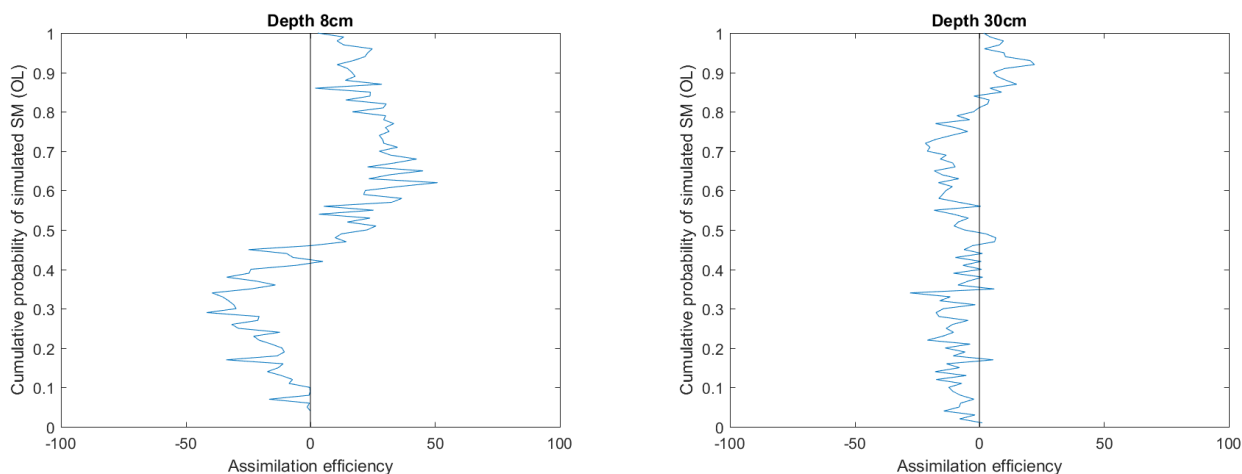

Figure 9. Assimilation efficiency as a function of simulated soil moisture quantiles: upper soil layer (right panel) and deeper soil layer (right panel).

3.4   Effect of the assimilation on predicted evapotranspiration

15 As evapotranspiration is also an important control in soil moisture dynamics, we propose to further evaluate the influence of the assimilation of SMOS observations on the monthly prediction of evapotranspiration. To do so, we compared the open loop and analysis simulations of monthly evapotranspiration with *in situ* observations derived from the flux towers (TERN OzFlux measurement network, http://www.ozflux.org.au/). Evapotranspiration observations are derived from monthly averaged flux tower measurements of latent heat flux. The comparison between observations and simulation results is carried out at the

Hydrology and
Earth System
Sciences
Discussions

Table 3. Time-space average values of background and analysis performances of evapotranspiration predictions (comparison with *in situ*-observed evapotranspiration).

	Correlation	RMSD	ubRMSD
background	0.46	0.057	0.034
analysis	0.48	0.056	0.034

grid cells including the flux towers. The spatially averaged performance metrics yielded by this comparison are reported in Table 3, which revealed that the predictions of evapotranspiration are improved by the assimilation of SMOS observations as the correlation with *in situ* observations increased by 0.02 with a marginal reduction in RMSD.
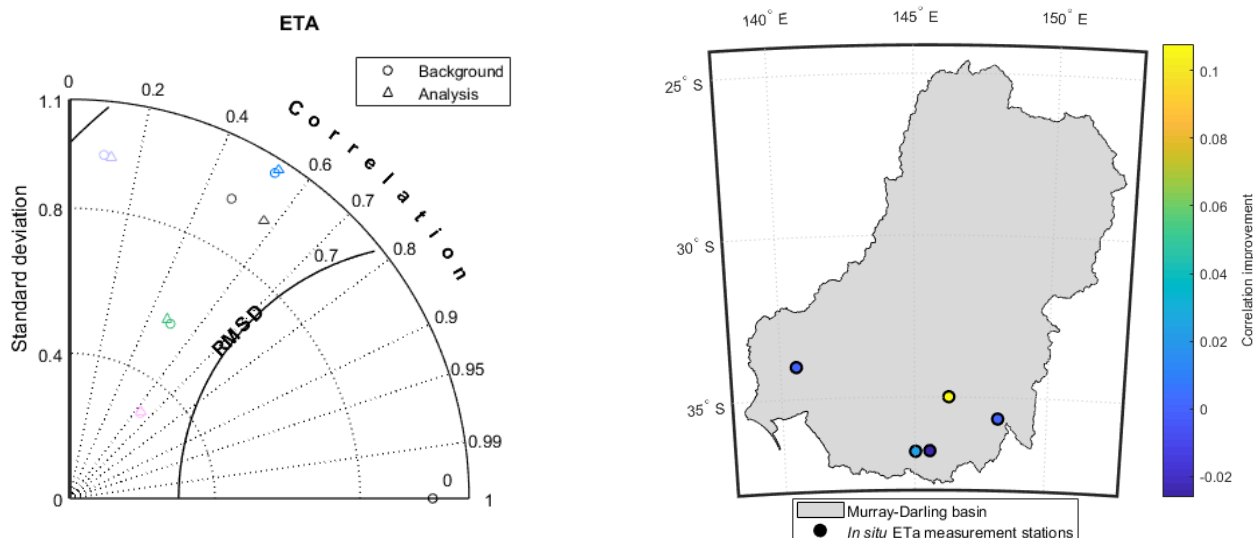

Figure 10. Effect of the assimilation on simulated evapotranspiration: Taylor Diagram drawn from the comparison between *in situ*-observed and SFX-simulated evapotranspiration (Background and analysis, left panel) and map of the correlation improvement in evapotranspiration (right panel).

Figure 10 shows the Taylor diagram as well as the map of correlation improvement for individual measurement stations. The effect of the assimilation on evapotranspiration is substantially positive for one station, limited for 3 of them and slightly negative for the last one. Figure 11 shows the percentage improvement of simulated monthly evapotranspiration as a results of SMOS Tb for each individual flux tower measurement together with averaged monthly rainfall (simulated by ERA-Interim). The percentage improvement is computed as follows:

$$Imp(t) = \frac{\|Ea_{OL}(t) - Ea_{Obs}(t)\| - \|Ea_{An}(t) - Ea_{Obs}(t)\|}{\|Ea_{OL}(t) - Ea_{Obs}(t)\|} * 100 \qquad (9)$$
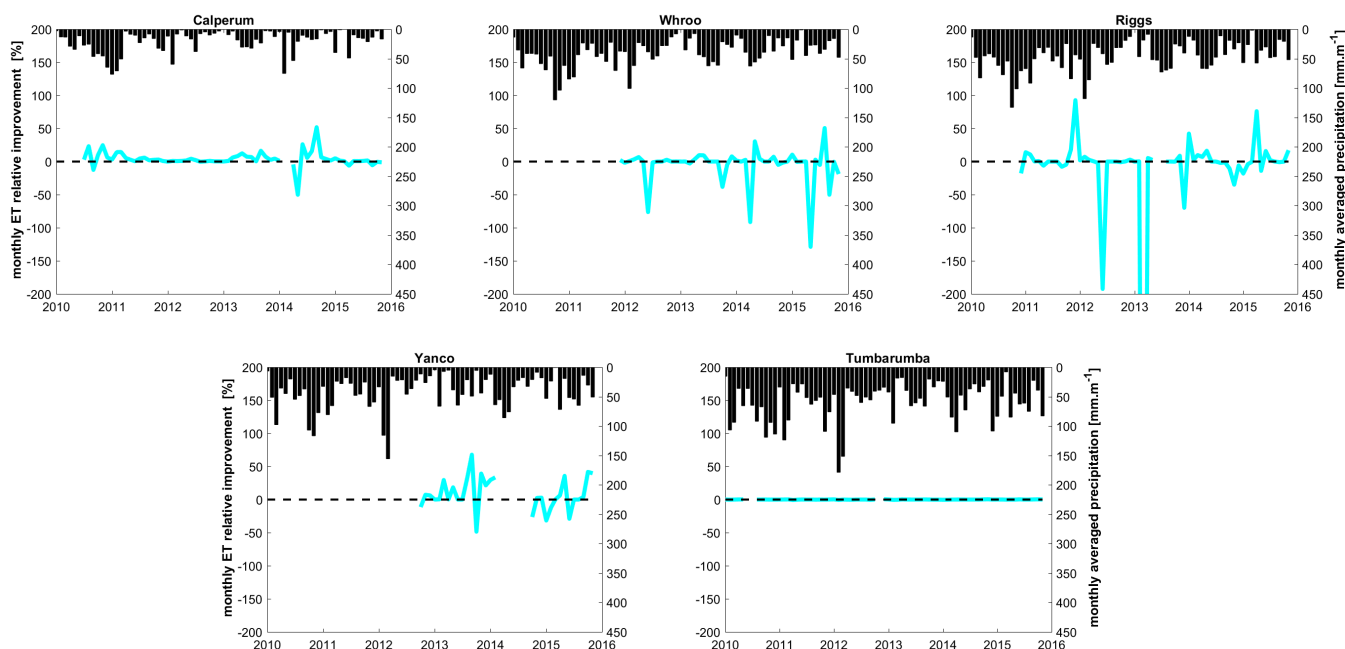
Figure 11. Effect of the assimilation on simulated evapotranspiration: Monthly rainfall and percentage improvement of simulated monthly evapotranspiration as a results of SMOS Tb assimilation for each individual flux tower measurement (flux tower locations sorted from west (top left panel) to east (bottom right panel).

where t is the time step, Imp the percentage improvement and Ea_{Obs}, Ea_{OL} and Ea_{An} respectively the observed, background and analysis evapotranspiration.

The positive (resp. negative) percentage improvement values indicate that absolute errors are reduced (resp. increased) as a result of the assimilation of SMOS Tb. In Figure 11, the assimilation lead from time to time either to an increase or a reduction
5 of the error in simulated evapotranspiration. While the site having low annual precipitation (ca. 250 mm.yr^{-1} at Calperum) exhibited a quasi systematic improvement, sites having medium annual precipitation (between ca. 480 to 560 mm.yr^{-1} at Whroo, Riggs and Yanco) exhibited more contrasting results. The wettest site (ca. 720 mm.yr^{-1}a t Tubarumba) showed very limited effect of the assimilation on the absolute error in simulated evapotranspiration. This result is in agreement with other studies (e.g., Detto et al., 2006; Vivoni et al., 2008; Mallick et al., 2018) that showed that water limitations in arid and semi-arid
10 regions make evapotranspiration very sensitive to soil moisture variations, thereby explaining the fact that the assimilation of SMOS Tb is more efficient in reducing errors of simulated evapotranspiration in water-limited regions of the MDB.

4 Conclusions

This study introduces and evaluates a large-scale SM modelling chain that is based on and takes advantage of the assimilation of SMOS Tb into a spatially distributed conceptual hydrological model coupled with a radiative model transfer. The main

objective is to assess the performance of such a modelling chain and its associated data assimilation system and to compare it with that of a quasi-identical set up using the physically based CLM land surface model (Rains et al., 2017). A closely connected second objective is to evaluate whether a SM modelling chain, based on a conceptual hydrological model, is able to reach the same performance level as that of one based on a physically-based model, the main advantage of a conceptual model being its substantially lower computational demand.

To carry out our experiment, we use as a test case the Murray-Darling basin in Australia. To enable a meaningful comparison with the study of Rains et al. (2017), we set up a modelling chain using the procedure described in Rains et al. (2017). The hydrological model is, in our study, based on the SUPERFLEX (SFX) modelling framework and includes two stratified upper root zone soil layers conceptually representing soil layers of 7 and 21 cm depth, respectively. It uses as forcings time series of rainfall, air and soil temperature derived from the ERA-Interim reanalysis product. The hydrological model is spatially distributed, each grid cell covering an area of 0.25° by 0.25°. The CMEM radiative transfer model is coupled with SFX in order to simulate SMOS-like Tb. The SFX model parameters are first calibrated based on Monte-Carlo simulations using as a calibration dataset SMOS Tb observations acquired over a period of two years (2010-2011). Next, SMOS Tb observations acquired over the 6-year period 2010-2016 are sequentially assimilated into the SFX-CMEM modelling chain. For the assimilation experiment, we apply a Local Ensemble Transform Kalman Filter. To generate an ensemble of SMOS-like Tb, the meteorological forcings of the SFX-CMEM models derived from the ERA-interim dataset, namely the rainfall and the air and soil temperature time series, are randomly perturbed.

The following key conclusions can be drawn from our experiment:

1. A 6-year forward run of the SFX-based modelling chain reaches performance levels similar to those obtained with CLM both in terms of simulated Tb (comparison with SMOS data) and SM (comparison with *in situ* observation). The average correlations between simulated and SMOS observed Tb range between 0.62 and 0.72 for both models. The local correlations between simulated and *in situ* observed SM range between 0.3 and 0.8 for CLM and between 0.3 and 0.9 for SFX.

2. The assimilation of SMOS Tb observations into the SFX-based modelling chain increases the correlation between simulated and *in situ* observed SM by ca. 0.03.

3. The improvement in correlation between simulated and *in situ* observed SM as a result of the assimilation is slightly lower in our study than that obtained in Rains et al. (2017), but the correlation values are higher. As a result of the assimilation, the average correlations between simulated and *in situ* observed SM (top and deeper root zone soil layers) range between 0.65 and 0.68 for CLM and between 0.73 and 0.8 for SFX.

4. The assimilation of SMOS Tb observations reduces errors between simulated and *in situ* observed SM, especially for the highest SM values while it tends to increase them for lower SM values. For the upper layer, errors are reduced for SM values higher than the median. For the deeper layer, errors are reduced for quantiles higher than 80 %.

5. The assimilation of SMOS Tb observations increases correlation by 0.02 and marginally reduces errors between simulated and *in situ* observed evapotranspiration.

Overall, the study provides consistent empirical evidence that the SM modelling chain based on a conceptual hydrological model can reach and at times exceed the performance levels of a modelling chain based on a more physically based state of the art land surface model. Moreover, although the conceptual model needs to be calibrated, our experiment shows that this calibration can be carried out using only satellite data and has therefore the potential to be applicable to all areas where satellite data are reliable and informative.

Hydrology and
Earth System
Sciences
Open Access
EGU
Discussions

References

Al Bitar, A., Leroux, D., Kerr, Y. H., Merlin, O., Richaume, P., Sahoo, A., and Wood, E. F.: Evaluation of SMOS Soil Moisture Products Over Continental U.S. Using the SCAN/SNOTEL Network, IEEE Transactions on Geoscience and Remote Sensing, 50, 1572–1586, 2012.

Al-Yaari, A., Wigneron, J.-P., Kerr, Y., Rodriguez-Fernandez, N., O'Neill, P., Jackson, T., Lannoy, G. D., Bitar, A. A., Mialon, A., Richaume, P., Walker, J., Mahmoodi, A., and Yueh, S.: Evaluating soil moisture retrievals from ESA's SMOS and NASA's SMAP brightness temperature datasets, Remote Sens. Environ., 193, 257–273, 2017.

Andreadis, K. and Schumann, G.-P.: Estimating the impact of satellite observations on the predictability of large-scale hydraulic models, Adv. Water Resour., 73, 44–54, 2014.

Brocca, L., Melone, F., Moramarco, T., Wagner, W., Naeimi, V., Bartalis, Z., and Hasenauer, S.: Improving runoff prediction through the assimilation of the ASCAT soil moisture product, Hydrol. Earth Syst. Sci., 14, 1881–1893, 2010.

Brocca, L., Moramarco, T., Melone, F., Wagner, W., Hasenauer, S., and Hahn, S.: Assimilation of surface-and root-zone ASCAT soil moisture products into rainfall–runoff modeling, IEEE T. Geosci. Remote, 50, 2542–2555, 2012.

Champeaux, J. L., Masson, V., and Chauvin, F.: ECOCLIMAP: a global database of land surface parameters at 1 km resolution, Meteorol. Appl., 12, 29–32, 2005.

Chen, F., Crow, W. T., and Ryu, D.: Dual forcing and state correction via soil moisture assimilation for improved rainfall–runoff modeling, J. Hydrometeorol., 15, 1832–1848, 2014.

Choudhury, B., Schmugge, T. J., Chang, A., , and Newton, R.: Effect of surface roughness on the microwave emission from soils, J. Geophys. Res.-Oceans, 84, 5699–5706, 1979.

De Lannoy, G. and Reichle, R.: Assimilation of SMOS brightness temperatures or soil moisture retrievals into a land surface model, Hydrol. Earth Syst. Sci., 20, 4895–4911, 2016a.

De Lannoy, G. J. M. and Reichle, R. H.: Global assimilation of multiangle and multipolarization SMOS brightness temperature observations into the GEOS-5 Catchment Land Surface Model for soil moisture estimation, J. Hydrometeorol., 17, 669–691, 2016b.

De Lannoy, G. J. M., Reichle, R. H., Houser, P. R., Pauwels, V., and Verhoest, N. E.: Correcting for forecast bias in soil moisture assimilation with the ensemble Kalman filter, Water Resour. Res., 43, W09 410, 2007.

de Rosnay, P., Drusch, M., Boone, A., Balsamo, G., Decharme, B., Harris, P., Kerr, Y., Pellarin, T., Polcher, J., and Wigneron, J.-P.: AMMA Land Surface Model Intercomparison Experiment coupled to the Community Microwave Emission Model: ALMIP-MEM, J. Geophys. Res.-Atmos., 114, D05 108, 2009.

Dee, D., Uppala, S., Simmons, A., Berrisford, P., Poli, P., Kobayashi, S., Andrae, U., Balmaseda, M., Balsamo, G., Bauer, P., Bechtold, P., Beljaars, A., van de Berg, L., Bidlot, J., Bormann, N., Delsol, C., Dragani, R., Fuentes, M., Geer, A., Haimberger, L., Healy, S., Hersbach, H., Hólm, E., Isaksen, L., Kållberg, P., Köhler, M., Matricardi, M., McNally, A., Monge-Sanz, B., Morcrette, J.-J., Park, B.-K., Peubey, C., de Rosnay, P., Tavolato, C., Thépaut, J.-N., and Vitart, F.: The ERA-Interim reanalysis: configuration and performance of the data assimilation system., Q. J. R. Meteorol. Soc., 137, 553 – 597, 2011.

Detto, M., Montaldo, N., Albertson, J. D. Mancini, M., and Katul, G.: Soil moisture and vegetation controls on evapotranspiration in a heterogeneous Mediterranean ecosystem on Sardinia, Italy, Water Resour. Res., 42, W08 419, 2006.

Devia, G., Ganasri, B., and Dwarakish, G.: A review on hydrological models, Aquatic Procedia, 4, 1001–1007, 2015.

Dharssi, I., Bovis, K. J., Macpherson, B., and Jones, C. P.: Operational assimilation of ASCAT surface soil wetness at the Met Office, Hydrol. Earth Syst. Sci., 15, 2729—2746, 2011.

Draper, C., Mahfouf, J.-F., and Walker, J.: An EKF assimilation of AMSR-E soil moisture into the ISBA land surface scheme, J. Geophys. Res.-Atmos., 114, D20 104, 2009.

Draper, C., Mahfouf, J.-F., Calvet, J.-C., Martin, E., and Wagner, W.: Assimilation of ASCAT near-surface soil moisture into the SIM hydrological model over France, Hydrol. Earth Syst. Sci., 15, 3829–3841, 2011.

5 Draper, C. S., Reichle, R. H., De Lannoy, G. J. M., and Liu, Q.: Assimilation of passive and active microwave soil moisture retrievals, Geophys. Res. Lett., 39, L04 401, 2012.

El Hassan, A. A., Sharif, H. O., Jackson, T., and Chintalapudi, S.: Performance of a conceptual and physically based model in simulating the response of a semi-urbanized watershed in San Antonio, Texas, Hydrol. Process., 27, 2013.

Entekhabi, D., Reichle, R. H., Koster, R. D., and Crow, W. T.: Performance Metrics for Soil Moisture Retrievals and Application Require-
10   ments, J. Hydrometeorol., 11, 832–840, 2010.

Ercolani, G. and Castelli, F.: Real-time variational assimilation of hydrologic and hydrometeorological data into operational hydrologic forecasting, Water Resour. Res., 53, 158–183, 2017.

Fenicia, F., Kavetski, D., and Savenije, H.: Elements of a flexible approach for conceptual hydrological modeling: 1. Motivation and theoretical development, Water Resour. Res., 47, W11510, 2011.

15 Fenicia, F., Kavetski, D., Savenije, H. H. G., and Pfister, L.: From spatially variable streamflow to distributed hydrological models: Analysis of key modeling decisions, Water Resour. Res., 52, 954–989, 2016.

García-Pintado, J., Mason, D. C., Dance, S. L., Cloke, H. L., Neal, J. C., Freer, J., and Bates, P. D.: Satellite-supported flood forecasting in river networks: A real case study, J. Hydrol., 523, 706 – 724, http://www.sciencedirect.com/science/article/pii/S0022169415001031, 2015.

20 Hamon, W.: Computation of direct runoff amounts from storm rainfall, IAHS-AISH P, 63, 52–62, 1963.

Holgate, C., De Jeu, R., van Dijk, A., Liu, Y., Renzullo, L., Vinodkumar, Dharssi, I., Parinussa, R., Schalie, R. V. D., Gevaert, A., Walker, J., McJannet, D., Cleverly, J., Haverd, V., Trudinger, C., and Briggs, P.: Comparison of remotely sensed and modelled soil moisture data sets across Australia, Remote Sens. Environ., 186, 479–500, 2016.

Hostache, R., Matgen, P., Montanari, A., Montanari, M., Hoffmann, L., and Pfister, L.: Propagation of uncertainties in coupled hydro-
25   meteorological forecasting systems: A stochastic approach for the assessment of the total predictive uncertainty, Atmos. Res., 100, 263 – 274, 2011.

Hostache, R., Matgen, P., Giustarini, L., Teferle, F., Tailliez, C., Iffly, J.-F., and Corato, G.: A drifting GPS buoy for retrieving effective riverbed bathymetry, J. Hydrol., 520, 397 – 406, 2015.

Hostache, R., Chini, M., Giustarini, L., Neal, J., Kavetski, D., Wood, M., Corato, G., Pelich, R.-M., and Matgen, P.: Near-Real-Time Assim-
30   ilation of SAR-Derived Flood Maps for Improving Flood Forecasts, Water Resour. Res., 54, 5516–5535, 2018.

Hunt, B. R., Kostelich, E. J., and Szunyogh, I.: Efficient data assimilation for spatiotemporal chaos: A local ensemble transform Kalman filter, Physica D, 230, 112–126, 2007.

Jia, B., Xie, Z., Tian, X., and Shi, C.: A soil moisture assimilation scheme based on the ensemble Kalman filter using microwave brightness temperature, Sci. China Ser. D, 52, 1835—1848, 2009.

35 Kerr, Y. H., Waldteufel, P., Wigneron, J. P., Martinuzzi, J., Font, J., and Berger, M.: Soil moisture retrieval from space: the Soil Moisture and Ocean Salinity (SMOS) mission, IEEE T. Geosci. Remote, 39, 1729–1735, 2001.

Kerr, Y. H., Waldteufel, P., Richaume, P., Wigneron, J. P., Ferrazzoli, P., Mahmoodi, A., Bitar, A. A., Cabot, F., Gruhier, C., Juglea, S. E., Leroux, D., Mialon, A., and Delwart, S.: The SMOS Soil Moisture Retrieval Algorithm, IEEE T. Geosci. Remote, 50, 1384–1403, 2012.

Lehner, B., Döll, P., Alcamo, J., Henrichs, T., and Kaspar, F.: Estimating the impact of global change on flood and drought risks in Europe: A continental integrated analysis, Climatic Change, 75, 273–299, 2016.

Lievens, H., De Lannoy, G., Al Bitar, A., Drusch, M., Dumedah, G., Hendricks Franssen, H.-J., Kerr, Y., Tomer, S., Martens, B., Merlin, O., Pan, M., Roundy, J., Vereecken, H., Walker, J., Wood, E., Verhoest, N., and Pauwels, V.: Assimilation of SMOS soil moisture and
5   brightness temperature products into a land surface model, Remote Sens. Environ., 180, 292–304, 2016.

Liu, Y. and Gupta, H. V.: Uncertainty in hydrologic modeling: Toward an integrated data assimilation framework, Water Resour. Res., 43, 1–18, W07401, 2007.

Lü, H., Crow, W., Zhu, Y., Ouyang, F., and Su, J.: Auto-calibration system developed to assimilate AMSR-E data into a land surface model for estimating soil moisture and the surface energy budget, Remote Sens., 8, 1–20, 2016.

10   Mallick, K., Toivonen, E., Trebs, I., Boegh, E., Cleverly, J., Eamus, D., Koivusalo, H., Drewry, D., Arndt, S., Griebel, A., Beringer, J., and Garcia, M.: Bridging thermal infrared sensing and physically-based evapotranspiration modeling: From theoretical implementation to validation across an aridity gradient in Australian ecosystems., Water Resour. Res., 54, 3409–3435, 2018.

Matgen, P., Fenicia, F., Heitz, S., Plaza, D., de Keyser, R., Pauwels, V., Wagner, W., and Savenije, H.: Can ASCAT-derived soil wetness indices reduce predictive uncertainty in well-gauged areas? A comparison with in situ observed soil moisture in an assimilation application,
15   Advances in Water Resources, 44, 49–65, 2012.

MDBA, T.: http://www.mdba.gov.au, accessed: 2018-10-09, 2018.

Mironov, V. L., Dobson, M. C., Kaupp, V. H., Komarov, S. A., and Kleshchenko, V. N.: Generalized refractive mixing dielectric model for moist soils, IEEE Trans. Geosci. Remote Sens., 42, 773–785, 2004.

Miyoshi, T. and Yamane, S.: Local Ensemble Transform Kalman Filtering with an AGCM at a T159/L48 Resolution, Mon. Weather Rev.,
20   135, 3841—3861, 2007.

Mohanty, B. P., Cosh, M. H., Lakshmi, V., and Montzka, C.: Soil Moisture Remote Sensing: State-of-the-Science, Vadose Zone J., 16, 1–9, 2017.

Moradkhani, H.: Hydrologic Remote Sensing and Land Surface Data Assimilation, Sensors, 8, 2986–3004, 2007.

Pappenberger, F., Frodsham, K., Beven, K., Romanowicz, R., and Matgen, P.: Fuzzy set approach to calibrating distributed flood inundation
25   models using remote sensing observations, Hydrol. Earth Syst. Sci., 11, 739–752, 2007.

Parada, L. M. and Liang, X.: Optimal multiscale Kalman filter for assimilation of near-surface soil moisture into land surface models, J. Geophys. Res.-Atmos., 109, D24 109, 2004.

Peischl, S., Walker, J. P., Rüdiger, C., Ye, N., Kerr, Y. H., Kim, E., Bandara, R., , and Allahmoradi, M.: The AACES field experiments: SMOS calibration and validation across the Murrumbidgee River catchment, Hydrol. Earth Syst. Sci., 16, 1697–1708, 2012.

30   Pellarin, T., Wigneron, J. P., Calvet, J. C., Berger, M., Douville, H., Ferrazzoli, P., Kerr, Y. H., Lopez-Baeza, E., Pulliainen, J., Simmonds, L. P., and andWaldteufel, P.: Two-year global simulation of L-band brightness temperatures over land,, IEEE Trans. Geosci. Remote Sens., 41, 2135–2139, 2003.

Rains, D., Han, X.and Lievens, H., Montzka, C., and Verhoest, N.: SMOS brightness temperature assimilation into the Community Land Model, Hydrol. Earth Syst. Sci., 21, 5929–5951, 2017.

35   Reichle, R. H., Koster, R. D., Liu, P., Mahanama, S. P., Njoku, E. G., and Owe, M.: Comparison and assimilation of global soil moisture retrievals from the Advanced Microwave Scanning Radiometer for the Earth Observing System (AMSR-E) and the Scanning Multichannel Microwave Radiometer (SMMR), J. Geophys. Res.-Atmos., 112, D09 108, 2007.

Renzullo, L. J., Van Dijk, A., Perraud, J.-M., Collins, D., Henderson, B., Jin, H., Smith, A., and McJannet, D.: Continental satellite soil moisture data assimilation improves root-zone moisture analysis for water resources assessment, J. Hydrol., 519, 2747–2762, 2014.

Revilla-Romero, B., Wanders, N., Burek, P., Salamon, P., and de Roo, A.: Integrating remotely sensed surface water extent into continental scale hydrology, J. Hydrol., 543, Part B, 659 – 670, 2016.

5   Smith, A. B., Walker, J. P., Western, A. W., Young, R. I., Ellett, K. M., Pipunic, R. C., Grayson, R. B., Siriwidena, L., Chiew, F. H. S., and Richter, H.: The Murrumbidgee Soil Moisture Monitoring Network Data Set, Water Resour. Res., 48, W07 701, 2012.

Su, C.-H., Ryu, D., Young, R. I., Western, A. W., and Wagner, W.: Inter-comparison of microwave satellite soil moisture retrievals over the Murrumbidgee Basin, southeast Australia, Remote Sens. Environ., 134, 1–11, 2013.

UNISDR: Sendaï Framework for Disaster Risk Reduction 2015-2030, Tech. rep., United Nations Office for Disaster Risk Reduction, 2015.

10 Vivoni, E. R., Moreno, H. A., Mascaro, G., Rodriguez, J. C., Watts, C. J., Garatuza-Payan, J., and Scott, R. L.: Observed relation between evapotranspiration and soil moisture in the North American monsoon region hydrologic forecasting, Geophys. Res. Lett., 35, L22 403, 2008.

Wanders, N., Karssenberg, D., de Roo, A., de Jong, S. M., and Bierkens, M. F. P.: The suitability of remotely sensed soil moisture for improving operational flood forecasting, Hydrol. Earth Syst. Sci, 18, 2343–2357, 2014.

15 Wigneron, J.-P., Laguerre, L., and Kerr, Y. H.: A simple parameterization of the L-band microwave emission from rough agricultural soils, IEEE Trans. Geosci. Remote Sens., 39, 1697–1707, 2001.

Wigneron, J.-P., Kerr, Y., Waldteufel, P., Saleh, K., Escorihuela, M.-J., Richaume, P., Ferrazzoli, P., De Rosnay, P., Gurney, R., Calvet, J.-C., Grant, J. P., Guglielmetti, M., Hornbuckle, B., Mätzler, C., Pellarin, T., , and Schwank, M.: L-band microwave emission of the biosphere (L-MEB) model: Description and calibration against experimental data sets over crop fields, Remote Sens. Environ., 107, 639—655, 2007.

20 Wood, M., Hostache, R., Neal, J., Wagener, T., Giustarini, L., Chini, M., Corato, G., Matgen, P., and Bates, P.: Calibration of channel depth and friction parameters in the LISFLOOD-FP hydraulic model using medium resolution SAR data and identifiability techniques., Hydrol. Earth Syst. Sci, 20, 4983–4997, 2016.

Yang, K., Watanabe, T., Koike, T., Li, X., Fujii, H., Tamagawa, K., Ma, Y., and Ishikawa, H.: Auto-calibration system developed to assimilate AMSR-E data into a land surface model for estimating soil moisture and the surface energy budget, J. Meteorol. Soc. Jpn. Ser. II, 85, 229–242, 2007.